World Electric Vehicle Journal

MDPI

Article

Comparative Analysis of Neural Network Models for Predicting Battery Pack Safety in Frontal Collisions

Jun Wang [1], Ouyang Chen [1], Zhenfei Zhan [1,*], Zhiwei Zhao [2] and Huanhuan Bao [2]

[1] School of Mechatronics and Vehicle Engineering, Chongqing Jiaotong University, Chongqing 400074, China; 622240800008@mails.cqjtu.edu.cn (J.W.); 622220990017@mails.cqjtu.edu.cn (O.C.)
[2] China Automotive Engineering Research Institute Co., Ltd., Chongqing 401122, China; zhaozhiwei@caeri.com.cn (Z.Z.); baohuanhuan@caeri.com.cn (H.B.)
* Correspondence: zhenfeizhan@cqjtu.edu.cn

Abstract: Amid concerns about environmental degradation and the consumption of non-renewable energy, the development of electric vehicles (EVs) has accelerated, with increasing focus on safety. On the road, battery packs are exposed to potential risks from unforeseen objects that may collide with or scratch the system, which may lead to damage or even explosions, thus endangering the safety of transportation participants. In this study, several predictive models aimed at assessing the safety performances of battery packs are proposed to provide a basis for data-driven structural optimization by numerically simulating the deformation of the battery base plate. Initially, a finite element model of the battery pack was developed, and the accuracy of the model was verified by performing modal analysis with various commercial software tools. Then, representative samples were collected using optimal Latin hypercube sampling, followed by collision simulations to gather data under different collision conditions. Next, the prediction accuracy of three models—PSO-BP neural network, RIME-BP neural network, and RBF neural network—was compared for predicting battery pack bottom shell deformation. Finally, the prediction accuracy of the models was compared based on error functions. The results indicate that these neural network models can accurately predict deformation under frontal collision conditions within the specified limits, with the RIME-BP model yielding the best performance beyond those limits. The developed neural network prediction model is able to accurately assess the mechanical response of battery packs under frontal collision, providing support for data-driven structural optimization. It also provides an important reference for improving the safety and durability of battery pack design.

Keywords: machine learning; collision simulation; safety performance prediction

check for updates

Academic Editor: Michael Fowler

Received: 16 December 2024
Revised: 14 January 2025
Accepted: 24 January 2025
Published: 5 February 2025

Citation: Wang, J.; Chen, O.; Zhan, Z.; Zhao, Z.; Bao, H. Comparative Analysis of Neural Network Models for Predicting Battery Pack Safety in Frontal Collisions. *World Electr. Veh. J.* **2025**, *16*, 78. https://doi.org/10.3390/wevj16020078

Copyright: © 2025 by the authors. Published by MDPI on behalf of the World Electric Vehicle Association. Licensee MDPI, Basel, Switzerland. This article is an open access article distributed under the terms and conditions of the Creative Commons Attribution (CC BY) license (https://creativecommons.org/licenses/by/4.0/).

1. Introduction

In recent years, China's new energy vehicle (NEV) industry has been growing rapidly thanks to strong government support, including subsidy policies, green development strategies, and efforts in reducing carbon emissions. At the same time, continuous advancements in technology have laid a solid foundation for the development of battery technologies, charging infrastructure, and the widespread adoption of intelligent electric vehicles. It is expected that the market penetration of NEVs will continue to rise in the coming years [1,2]. The safety of the battery is directly related to the overall performance and market acceptance of electric vehicles, especially in extreme operating conditions, such as high temperatures, cold environments, and collisions. If a battery pack undergoes thermal runaway, swelling, or explosion due to collisions, overcharging, overdischarging,

short circuits, or other mechanical impacts, it not only leads to economic losses but may also pose serious risks to human life and safety. Therefore, enhancing the safety of battery packs has become a top priority in the NEV industry [3–5], and researchers have conducted extensive studies to ensure battery safety [6–8].

When subjected to mechanical shock, batteries may experience thermal runaway phenomenon, which can cause safety accidents [9]. Many studies have been conducted on the failure mode of batteries after impact [10–12].Li et al. investigated the failure mechanisms of square lithium iron phosphate ($LiFePO_4$) batteries under vibration conditions. They found that, although the batteries underwent slight deformation, their performance remained stable without significant safety hazards, indicating that $LiFePO_4$ batteries exhibit good safety and reliability in the vibration environment of electric vehicles [13]. Zhu et al. analyzed the thermal runaway (TR) characteristics of $LiFePO_4$ batteries through thermal runaway experiments and simulation models. Their study revealed that the heat released from the negative electrode-electrolyte reaction is the primary heat source, accounting for 63.1% of the total heat generation during the thermal runaway process [14]. Shi et al. introduced a transfer learning approach that predicts heat release variability during TR in lithium-ion batteries. By using mass ejection data and metadata, this method reduces the time and cost of assessing thermal risks, providing a more efficient way to evaluate Li-ion battery safety [15]. Wang et al. investigated an optimized design for a non-modular battery pack with a negative Poisson's ratio, balancing volumetric energy density, impact resistance, and heat dissipation performance. The research demonstrated that materials with a negative Poisson's ratio significantly enhance the side-pole impact resistance of the battery pack [16]. Kisters et al. revealed the significant impact of the presence and thickness of the electrolyte on the dynamic response of lithium-ion batteries. Their findings showed that hard-shell and soft-shell batteries exhibit different failure modes under high-speed loading conditions, providing important insights for improving battery pack design [17]. Zhang et al. used FEM simulations and machine learning to study battery pack safety under cone impact, examining factors like radius, shell condition, and velocity. Their models showed strong performance, particularly in real-time and noisy conditions, demonstrating the potential of combining machine learning with FEM for safer battery pack design. [18].

Currently engineers usually start with extensive crash analysis when designing a battery pack system (BPS) [19–21]. These collision simulations are often very time-consuming when multiple design variables are considered. By using machine learning algorithms to build a predictive model of the mechanical response, the response variables can be obtained directly, which can significantly reduce the time required for data collection. Xu et al. investigated the effectiveness of five different machine learning algorithms, including CS-BP, PSO-RBF, WOA-SVM, BES-ELM, and GWO-LSTM, in predicting the mechanical response of a battery pack under bottom collision conditions, demonstrating the feasibility of applying machine learning techniques to such predictive tasks [22]. Li et al. further compared the accuracy of neural networks (NNs) with traditional machine learning algorithms, such as support vector machines (SVMs), in predicting the mechanical response of battery packs under low-speed frontal collision conditions [23]. Their results revealed that the neural network model significantly outperformed traditional algorithms in terms of prediction accuracy, particularly in capturing the deformation behavior of the battery pack's bottom shell. Inspired by these findings, this study explores the performance of three distinct neural network models in predicting the mechanical response of battery packs under frontal collision scenarios, aiming to further enhance prediction accuracy and robustness.

In order to reduce the simulation cost as well as to provide valuable data for optimizing the battery pack design, several neural network-based prediction models are presented

in this paper. The focus of this study is on the safety of the battery pack system (BPS) during frontal collisions, and simulation data on the deformation of the battery pack base plate under different collision scenarios were collected. First, a finite element model of the BPS was developed and its validity was verified using three software packages. Then, prediction models based on particle swarm optimization–backpropagation (PSO-BP), rime optimization algorithm–backpropagation (RIME-BP), and radial basis function artificial neural networks (RBF-ANNs) were developed and their prediction accuracies were evaluated. The effectiveness of these models is further validated. The main contributions of this study are as follows:

- Relationships between bottom shell deformation and shell thickness, collision velocity, and obstacle radius were established.
- We evaluated the accuracy of the proposed prediction models.
- The accuracy of the models in predicting results outside the specified range was examined.

The structure of the paper is organized as follows: Section 2 details the development and validation of the nonlinear finite element model of the BPS, followed by collision simulations. Section 3 introduces the neural network-based predictive models. In Section 4, the prediction accuracy of the various models is evaluated based on simulation and model results. Section 5 concludes with a summary of the findings.

2. Finite Element Modeling and Data

Conducting physics experimentation usually requires a lot of resources. However, thanks to the rapidly developing finite element method, today's specialized software can efficiently and accurately simulate realistic physical phenomena on computers. The process of building a finite element model of a battery pack and the implementation of collision simulation are described as the focus of this section.

2.1. Finite Element Analysis of BPS

Figure 1 illustrates the structure of the battery pack, which includes both the upper and lower enclosures. The lower shell, which is deformed by collisions during the experiment, is structurally composed of the bottom shell, bracket, and connecting bracket. The beams provide additional support for the overall stiffness of the battery pack. The height of the battery pack is 249 mm, the width is 834 mm, and the length is 1576 mm, and it contains 81 cell modules, which are modeled as homogenized solids with hexahedral cells for computational efficiency. Table 1 lists the thicknesses of the main components. As for the connections, the components of the battery pack are welded to the shell, while the bottom shell is bolted to the top shell.

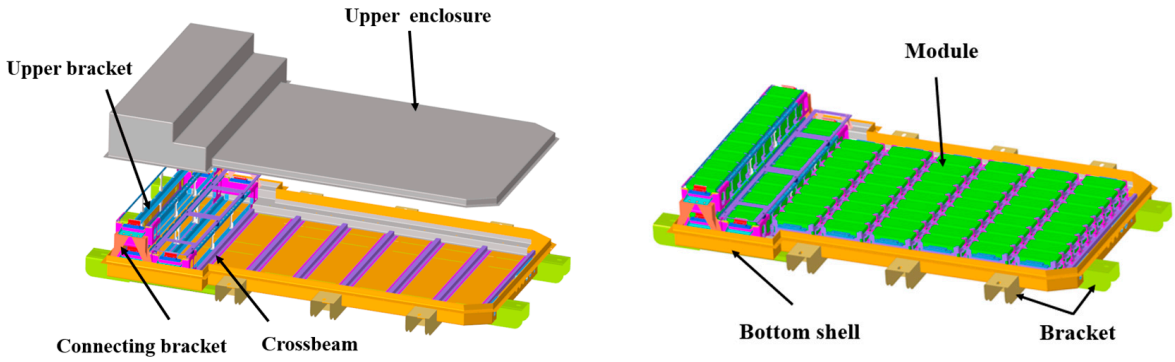


Figure 1. Finite element model of the BPS.

Table 1. Dimensions of the main components of the battery pack.

Component	Dimensions (mm)	Component	Dimensions (mm)
Bracket	3	Upper bracket	1.5
Upper enclosure	2	Crossbeam	1.8
Connecting bracket	1.8	Bottom shell	2

In order to ensure the credibility and reliability of the finite element models, they need to be validated. The quality of the elements was initially assessed by verifying their warping, tilting, Jacobi, and aspect ratios through computer-aided calibration. The model primarily consists of 836,874 shell elements, each with 6 mm dimensions. Of these, 801,416 (98.5%) are quadrilateral elements, and 12,673 (1.5%) are triangular elements. The quality indicators of all elements meet the required standards, confirming the whole quality of the model.

To verify the validity of the simulation model, numerous studies applying numerical methods have been conducted [24]. In this paper, constrained modal analysis of the finite element model is performed using Optistruct, Ansys, and Abaqus. Circular holes on each lug are used as constraint locations to simulate the operation of the battery pack suspended from the frame. The modal vibration patterns of the 1st to 7th order battery pack models are consistent across the three packages, and the vibration frequencies are shown in Table 2. The results of constrained modal analysis from different software packages show that the first to seventh order vibration frequencies are basically the same. The largest error occurs in the fourth-order frequency, at 4.79%, which is within acceptable limits for most engineering applications. The validity of the finite element model can be illustrated by the above results, which are suitable for simulating frontal collisions.

Table 2. The intrinsic frequency obtained from the software.

Orders	Abaqus (Hz)	Ansys (Hz)	Error (%)	Optistruct (Hz)	Error (%)
1	19.91	19.71	1	20.03	0.6
2	22.62	23.46	3.71	23.54	4.07
3	23.94	23.77	0.71	23.23	2.97
4	26.70	25.76	3.52	27.98	4.79
5	29.56	30.15	2	30.33	2.6
6	33.74	32.82	2.73	32.61	3.35
7	38.63	40.27	4.25	37.59	2.69

2.2. Collision Simulation Conditions

The frontal crash simulation of the battery pack was performed using Abaqus software. In this simulation, the battery pack collides with a stationary obstacle at a specified initial velocity. Automatic face-to-face contact is implemented, with static and dynamic friction coefficients set at 0.2 and 0.1, respectively. To avoid volume locking and zero-energy deformation modes, a stiffness-based hourglass control method is employed [25–27]. The material used for the battery pack's bottom shell is DP980 steel, with the failure criterion for DP980 steel defined by a maximum equivalent plastic strain of 20%, which simulates its fracture behavior under realistic conditions [23]. We made the following assumptions for the simulations: (a) the obstacle is treated as a rigid, fixed body; (b) the battery pack is allowed to move only in the direction of the vehicle's velocity; (c) the battery module is modeled as an isotropic homogeneous material.

The actual collision process will be affected by a variety of factors, and this paper focuses on the impact of collision speed, chassis thickness, and obstacle size on the deformation behavior of the battery pack. The road traffic laws of the People's Republic of China stipulates that vehicles need to travel at a speed of less than 30 km per hour when

driving on muddy, low-visibility, or other dangerous roads. In the simulation, a cylinder is chosen as the collision obstacle. Based on the test criteria and considerations for lightweight design [28], five ratings were defined for each factor: crash speed, thickness, and radius of obstacles. The specific levels for each parameter are detailed in Table 3. Figure 2 shows the working conditions and chassis deformation during a frontal collision of the battery pack. To simulate the fixed position of the battery pack on the vehicle, the collision is applied at the center between the two front ears of the battery pack. In Figure 2a the simulated conditions of the collision are shown and in Figure 2b various colors represent the deformation during the collision.

Table 3. Five different levels of design variables.

Levels	Collision Velocity (Km/h)	Obstacle Radius (mm)	Thickness of Bottom Shell (mm)
1	20	40	2
2	24	50	2.2
3	28	60	2.4
4	32	70	2.6
5	36	80	2.8

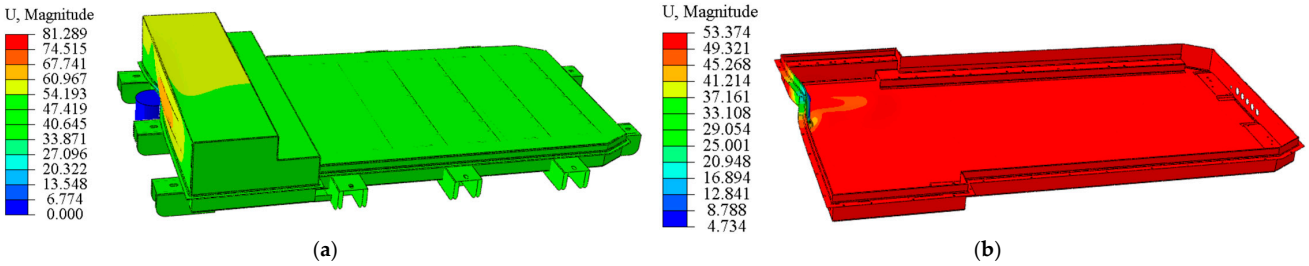


Figure 2. Deformation data and collision simulation condition. (**a**) Collision conditions at the front. (**b**) Deformation illustrated by colors.

3. Prediction Model

Finite element simulations can generally replicate real-world scenarios only to a limited extent. However, if the simulation results are used to establish a predictive model [29,30], the response values for the amount of bottom shell deformation can be quickly obtained. This approach not only ensures a reasonable level of prediction accuracy but also reduces the number of simulations, thereby enhancing work efficiency.

3.1. Experimental Design and Correlation Analysis

We present several neural network-based prediction models and evaluate the prediction accuracy of each model. The model development and selection process is depicted in Figure 3. We assess the prediction accuracies of these models within a specified range and beyond, analyzing neural network models including PSO-BP, RIME-BP, and RBF neural networks.

Optimal Latin hypercubic sampling was used as the experimental methodology used to obtain the experimental samples. In comparison, using a full factorial design would require 125 repetitions for a 3-factor, 5-level experiment. Optimal Latin hypercube sampling not only reduces the number of experiments necessary in large-scale studies but also ensures a more even distribution of sampling points across the input space than standard Latin hypercube sampling. This method minimizes sample bias, improves the reliability of output analysis, and is particularly effective for sensitivity analysis and uncertainty assessment in high-dimensional variable spaces, as it thoroughly covers the complex input range [31,32],

The 50 sets of samples taken in this paper by the optimal Latin hypercube sampling method are shown in Table 4.

$$Ce_i = \left[co_i^{i-1}, co_i^i\right], i \in [1, m] \quad (1)$$

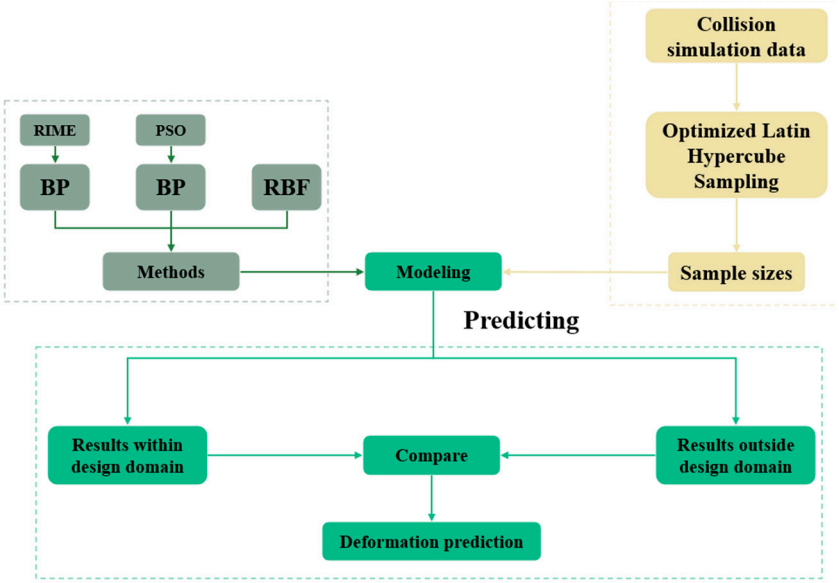


Figure 3. Methodology for constructing and choosing predictive models.

Table 4. Optimal Latin hypercube sampling results.

Run	Collision Velocity (Km/h)	Obstacle Radius (mm)	Thickness of Bottom Shell (mm)
#1	36	80	2.2
#2	36	80	2
#3	36	80	2.8
#4	36	80	2.6
#5	28	80	2
#6	24	80	2
#7	20	80	2.8
#8	20	80	2.2
#9	32	70	2.4
...	...	...	...
#50	24	40	2.4

In the above equation, *Ce* denotes a cell divided along the *co* dimensional coordinate, *co* denotes a dimensional coordinate in n-dimensional space, and *i* refers to a cell within m intervals. In order to achieve a random distribution of sample points within each cell, m points need to be randomly selected. It is more decentralized than ordinary cube sampling, ensuring that the sample points are not clustered together, which makes the sampling results more representative.

The predictive accuracy of the regression model is higher within the defined limits but beyond those limits. This paper addresses the issue of prediction accuracy both within and beyond the defined limits. First, we analyzed the correlation between collision velocity, obstacle radius, base plate thickness, and deformation, varying one variable at a time while keeping the other two variables constant. The effect of each variable on deformation was then observed. Figure 4 shows the relationship between the shell deformation and different factors. Figure 4a indicates that as the wall thickness increases, the deformation decreases. Figure 4b demonstrates that as the collision velocity increases, the deformation increases. Figure 4c shows that the obstacle radius has no significant effect on the deformation. These

three figures highlight the varying impacts of wall thickness, velocity, and obstacle radius on the safety of the battery pack.

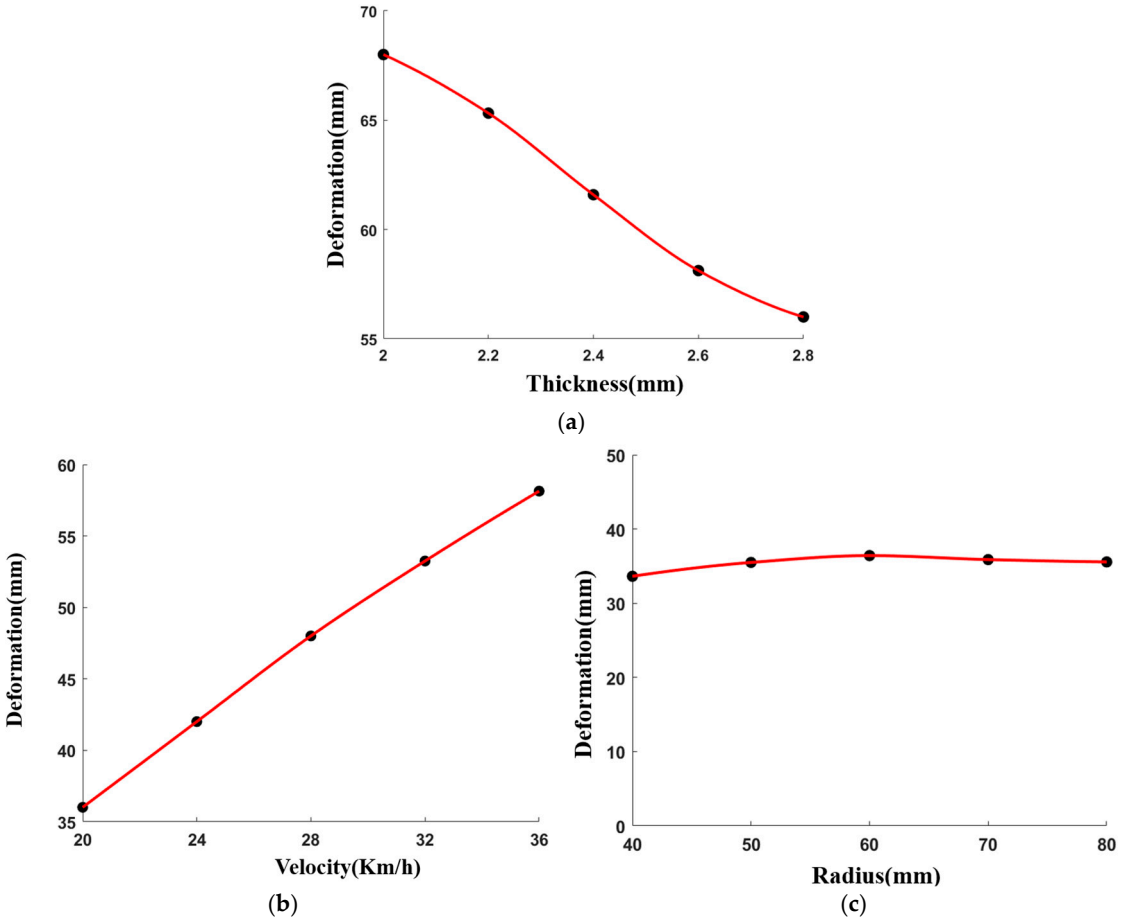


Figure 4. Effect of different factors on bottom shell deformation. (**a**) Effect of bottom shell thickness (mm) on deformation (mm). (**b**) Effect of collision velocity (km/h) on deformation (mm). (**c**) Effect of obstacle radius (mm) on deformation (mm).

We also use the correlation diagram shown in Figure 5 to study the relationship between different variables and the deformation of the battery pack bottom case. The correlation coefficient ranges from -1 to 1, indicating the strength and direction of the relationship between any two variables. A correlation coefficient of 1 indicates a perfect positive correlation, -1 indicates a perfect negative correlation, and 0 indicates no correlation. In the diagram, a more yellow color indicates a stronger positive correlation, while a grayer color represents a stronger negative correlation. A greener color indicates a weaker correlation. The correlation coefficients were calculated based on data from 50 simulation sets, with the exact values provided in the figure. The values in the last row represent the correlation between the amount of bottom shell deformation and each design variable. As shown in the figure, the correlation coefficient between collision velocity and deformation is about 0.89, which indicates a significant positive correlation between the two. The correlation coefficient between deformation and chassis thickness is -0.29, indicating a negative correlation between the two. The correlation between deformation and obstacle radius is very weak with a correlation coefficient of 0.03. In addition, the correlation coefficients between all the input variables are almost 0, which means that there is almost no linear relationship between the variables.

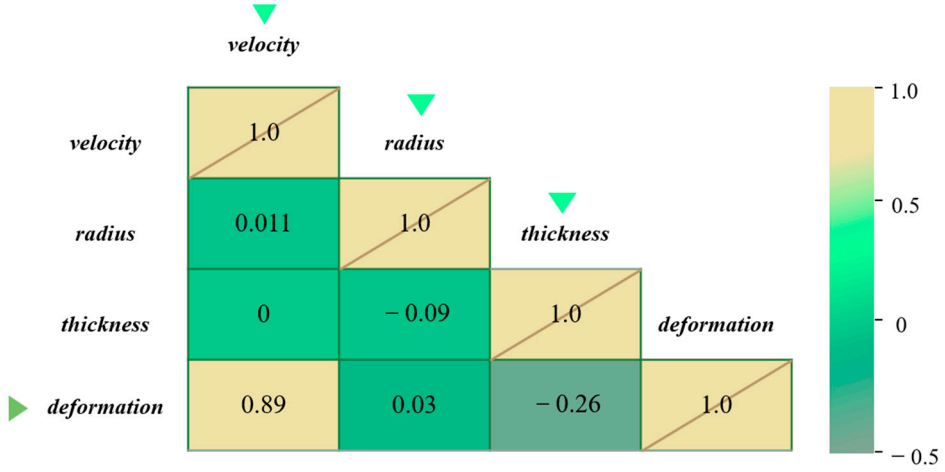


Figure 5. The correlation matrix of deformation and design variables.

3.2. PSO-BP

BP neural network, which stands for backpropagation neural network, operates by propagating signals through both forward and error backpropagation. It is composed of three or more layers, including the input, hidden, and output layers. In a neural network, information flows from the input layer through the hidden layer to the output layer. When the output deviates from the target, the error signal is propagated back through the hidden and input layers. Subsequently, the weights and biases between neurons are adjusted to gradually converge toward the desired outcome [33–35].

The following equation shows the corresponding iterative formula for the weights:

$$\Delta\omega_{ij}(n) = -\eta\frac{\partial E}{\partial\omega_{ij}(n)} + \alpha\Delta\omega_{ij}(n-1), n \in N^{+} \tag{2}$$

In Equation (2), the difference of the nth iteration weights is denoted by $\Delta\omega_{ij}(n)$, and the mean square error of the output layer is denoted by E. The first term is the regular learning factor term, which is a learning factor that can be set on a case-by-case basis. The first term is the regular learning factor term, and the second term is the momentum factor term. Before running the network algorithm, the sample data must be normalized to eliminate the effect of dimensionality among the variables [36].

$$X = \frac{x - min(A)}{max(A) - min(A)} \tag{3}$$

$$l = \sqrt{n + m + a} \tag{4}$$

In Equation (3), X denotes the value of the data after normalization, $X \in [-1, +1]$; $max/min(A)$ denotes the maximum number of data elements in the same column; a is all the elements of the same column; and X is the value of a particular number on that column. Backpropagation neural network implements the input-output mapping function. Mathematical theory proves that the three-layer neural network is capable of approximating nonlinear continuous functions with arbitrary accuracy.

The empirical formula of the neural network is shown in Equation (4); n is the number of neurons in the input layer, m is the number of neurons in the output layer, $a \in [1, 10]$, and the number of neurons in the hidden layer is denoted by l. In this study, the initial speed of the battery pack, the radius of the fixed rigid body, and the thickness parameter of the battery pack bottom case are selected as the neurons of the input layer of the network, and the deformation amount of the bottom case of the battery pack is selected as the neurons of

the output layer of the network, and the corresponding structure of the BP neural network prediction model is shown in Figure 6.

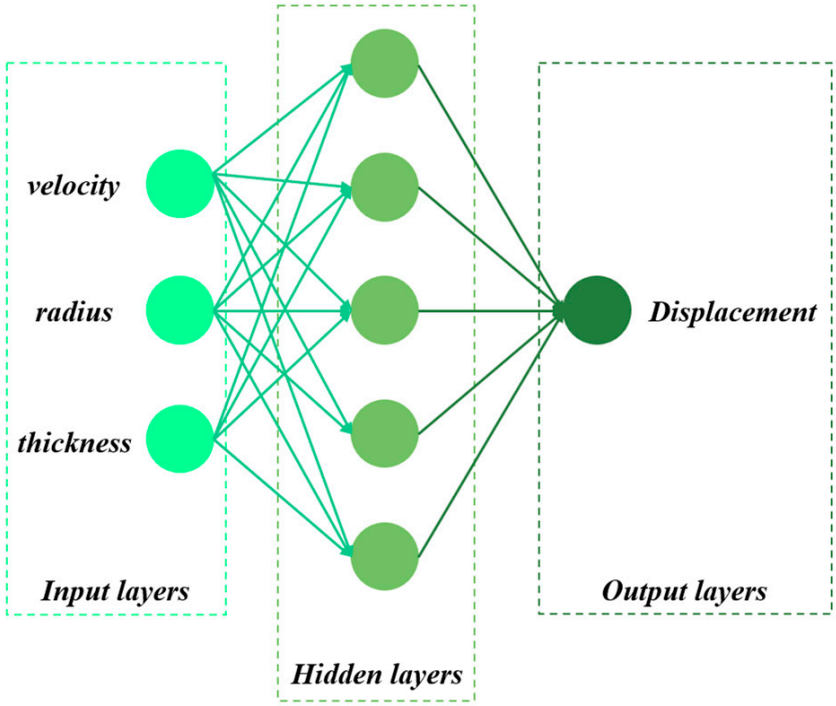


Figure 6. BP neural network structure.

Particle swarm optimization (PSO) is an intelligent optimization technique inspired by the natural behavior of birds. The method simulates the foraging behavior of birds, where they adjust their search paths based on both personal experience and communication with others. In the PSO algorithm, particles are initialized and iteratively update their speed and position based on individual and global best positions. Each particle remembers the optimal position of q_{gd} during iteration, and the optimal position of all particles is the global optimal position of q_{gd}. The formula for updating the velocity and position is as follows [33]:

$$v_{id}^{m+1} = w(m)v_{id}^{m} + c_1 r_1^m (q_{id} - x_{id}^m) + c_2 r_2^m \left(q_{gd} - x_{id}^m\right) \quad (5)$$

$$x_{id}^{m+1} = x_{id}^{m} + v_{id}^{m+1} \quad (6)$$

In the above equation i denotes a particle; m denotes the current iteration; d is the particle size; v_{id}^m and x_{id}^m are the velocity and position of the mth iteration; the non-negative constants c_1 and c_2 are the learning factors; r_1 and r_2 are arbitrary numbers distributed in the interval [0, 1]; and $w(m)$ is the inertia weighting factor.

The PSO-BP algorithm combines the advantages of PSO and BP and optimizes the initial weights and thresholds of the BP network by the particle swarm algorithm, which improves the performance and convergence speed of the BP neural network model. The training flowchart of the PSO- BP neural network prediction model built in this study is shown in Figure 7.

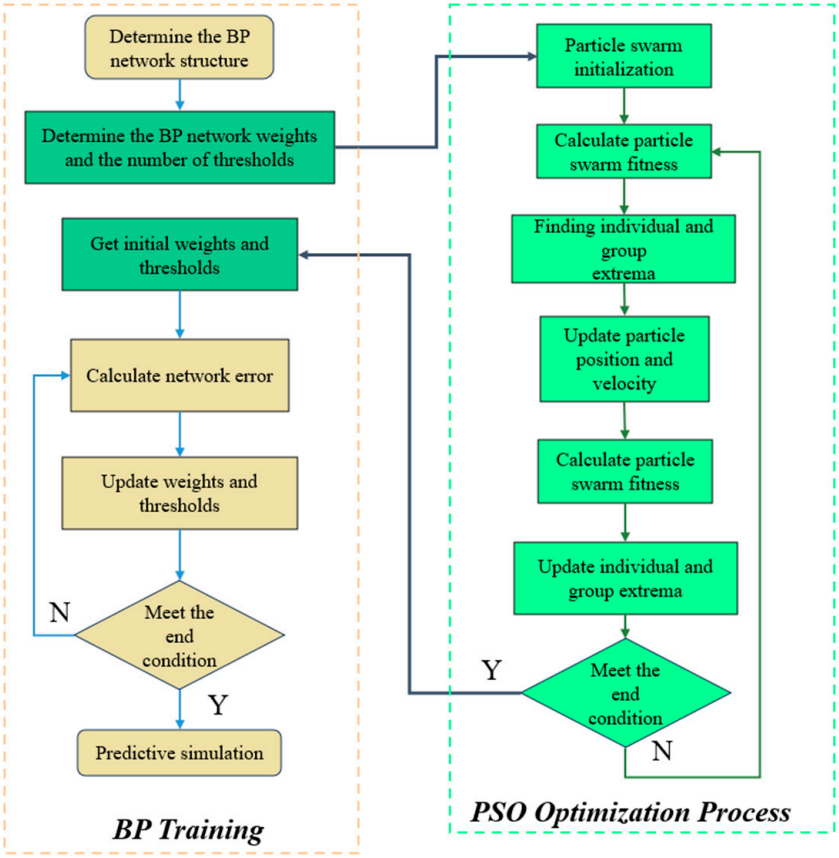


Figure 7. Training process of PSO-BP.

3.3. RIME-BP

In addition to the particle swarm optimization algorithms mentioned above, Su Huang et al. proposed a parameter-seeking optimization algorithm (RIME) based on the physical phenomenon of frost and ice [37]. RIME is a meta-heuristic algorithm based on the frost growth mechanism, which achieves optimization by simulating the growth behaviors of both soft-rime and hard-rime frosts. The algorithm consists of three main mechanisms: a soft-rime search strategy, a hard-rime puncturing mechanism, and an aggressive greedy selection mechanism. These mechanisms act synergistically in global search and local exploitation, which can effectively improve the solution performance of complex optimization problems. Compared with the classical algorithms, such as PSO, WOA, HHO and MFO, RIME converges quickly, can better balance the exploration and utilization of resources, and has a stronger ability to find the optimal solution and higher stability in the face of complex problems. The position update formula of the fog particles is as follows:

$$R_{ij}^{\text{new}} = R_{best,j} + r_1 \cdot \cos\theta \cdot \beta \cdot \left(h \cdot \left(Ub_{ij} - Lb_{ij}\right) + Lb_{ij}\right), \quad r_2 < E \tag{7}$$

$$\theta = \pi \cdot \frac{t}{10T} \tag{8}$$

$$\beta = 1 - \left(\frac{w \cdot t}{T}\right)/w \tag{9}$$

$$E = \sqrt{t/T} \tag{10}$$

where R_{ij}^{new} denotes the new position of the updated particle; i and j denote the ith time and the jth particle; $R_{\text{best},j}$ denotes the jth particle of the best fog agent in the fog population; r_1

and r_2 denote the random numbers; cos θ is the direction of the particle motion; β denotes the environmental factor; h is the adhesion degree; Ub_{ij} and Lb_{ij} are the upper and lower bounds of the escape space; t is the current number of iterations; T is the maximum number of iterations; and w denotes the number of segments of the step function.

In this paper, a RIME-BP neural network prediction model is built. The model optimizes the initial weights and thresholds of the BP neural network through the RIME optimization algorithm and overcomes the local optimum problem caused by the random initialization of the BP network by utilizing the global exploration ability and local exploitation mechanism of the RIME algorithm. In addition, the optimized parameters significantly accelerate the convergence of the BP network and improve the prediction accuracy and robustness of the traditional BP neural network prediction model. The training flowchart of the RIME-BP neural network prediction model constructed in this study is shown in Figure 8.

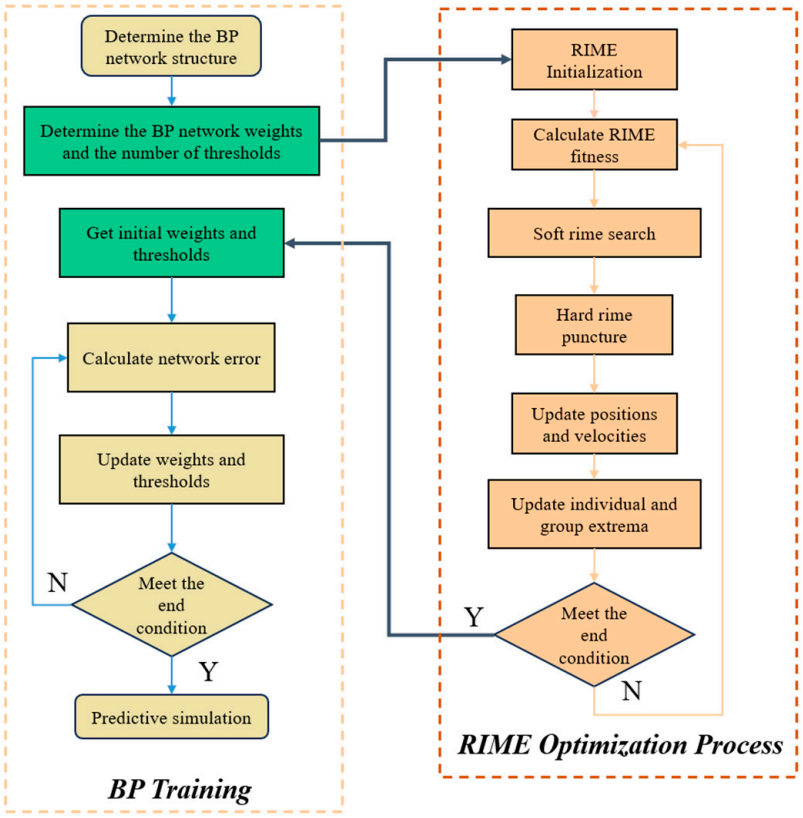


Figure 8. Training process of RIME-BP.

3.4. RBF-ANN

The RBF neural network is one of the most widely used prediction algorithms, consisting of fully connected input, hidden, and output layers. The network uses radial basis functions as hidden units, which constitute the hidden layer space. The RBF neural network nonlinearly maps the input data through the radial basis functions, maps the original low-dimensional input vector to the high-dimensional feature space, which improves the model's ability to fit the nonlinear problem, and sums the weighted outputs of the hidden units to obtain the output [38,39]. In this paper, a Gaussian function is used as the activation function of the hidden layer, and its expression is shown in Equation (11). The network output is obtained from the weighted Equation (12) [40].

$$\varphi_j(x) = \exp\left(-\frac{1}{2\sigma^2}\| x - c_j \|^2\right) \tag{11}$$

$$y = \sum_{j=1}^{p} \varphi_j \omega_j \tag{12}$$

where x is the input sample; $\| x - c_j \|$ represents the Euclidean distance between the input sample x and the center of the hidden layer node c_j; c_j is the center of the Gaussian function; σ is the variance of the Gaussian function; and ω_j denotes the weights between the hidden layer and the output layer, $j = 1, 2, 3, \ldots, p$. The model performance is optimized by adjusting the center and width of the hidden nodes to optimize the model performance and using linear least squares to quickly solve the output layer weights. RBF-ANN Since the hidden layer weights do not need iterative training, and the output layer weights can be quickly solved by the linear least squares method, it has the characteristics of fast convergence and easy adjustment of the parameters, and therefore it has been widely used in the fields of function approximation, classification, prediction, and so on.

4. Experimental Results

In this section, we will use various error metrics to assess the accuracy of different prediction models, including mean square error (MSE), mean absolute error (MAE), mean absolute percentage error (MAPE), root mean square error (RMSE), and coefficient of determination (R^2). These metrics quantify the performance of each model by comparing predicted outputs with actual simulation results.

For the training of neural network models, different error functions can be used as the loss function to guide the optimization process. In this study, we focus on using MSE as the primary loss function, which measures the average squared differences between the predicted and true values. It penalizes larger errors more heavily, making it suitable for problems where large deviations in prediction are undesirable. However, other error metrics such as MAE and MAPE can also be employed as loss functions, particularly when the goal is to minimize the absolute errors or the relative percentage errors between predictions and true values. While MSE is more sensitive to outliers, MAE provides a more robust measure when dealing with errors of similar magnitude, and MAPE is especially useful for percentage-based evaluations.

Once the models are trained, we use RMSE and R^2 to assess the overall performance of the models. RMSE is the square root of the mean squared error, providing a measure of the average magnitude of error in the same units as the predicted values, making it more interpretable in real-world contexts. R^2, on the other hand, indicates the proportion of variance in the target variable that is explained by the model, with values closer to 1.0 indicating better fit and prediction accuracy.

First, 50 representative sample sets were selected using optimal Latin hypercube sampling as described in Section 2, and the corresponding simulation results for these sets were obtained. These simulation results were then randomly divided into training, validation, and test sets in a ratio of 70%, 15%, and 15%, respectively. The training set was used to train the models, the validation set was used for hyperparameter tuning and monitoring overfitting, and the test set was used to evaluate the final performance of the models. To account for the inherent stochasticity in neural network training, five independent runs were performed for each neural network model. The results of these runs are presented in Tables 5–7. The differences between the neural network predictions and the simulation results are visualized in Figure 9. Finally, a comparison of the error metrics for each prediction model is provided in Figure 10.

Table 5. Training results of PSO-BP neural network model.

Run	R^2	MSE (mm^2)	RMSE (mm)	MAE (mm)	MAPE (%)
#1	0.9955	0.3846	0.6202	0.3638	0.7134
#2	0.9959	0.3688	0.6073	0.4837	0.99
#3	0.9954	0.3872	0.6223	0.3505	0.6880
#4	0.9958	0.3519	0.5932	0.3502	0.6896
#5	0.9959	0.3498	0.5914	0.3413	0.6712

Table 6. Training results of RIME-BP neural network model.

Run	R^2	MSE (mm)	RMSE (mm)	MAE (mm)	MAPE (%)
#1	0.9957	0.3577	0.5981	0.3701	0.7403
#2	0.9959	0.3424	0.5852	0.3481	0.6882
#3	0.9956	0.3706	0.6088	0.3641	0.7212
#4	0.9955	0.3730	0.6108	0.3465	0.6830
#5	0.9955	0.3828	0.6187	0.3839	0.7594

Table 7. Training results of RBF-ANN neural network model.

Run	R^2	MSE (mm)	RMSE (mm)	MAE (mm)	MAPE (%)
#1	0.9776	1.6677	1.2914	0.91967	1.891
#2	0.9786	1.7463	1.3215	0.95947	1.973
#3	0.9825	1.5404	1.2411	0.90358	1.908
#4	0.9813	1.5248	1.2348	0.89061	1.861
#5	0.9775	1.8639	1.3652	1.0023	2.082

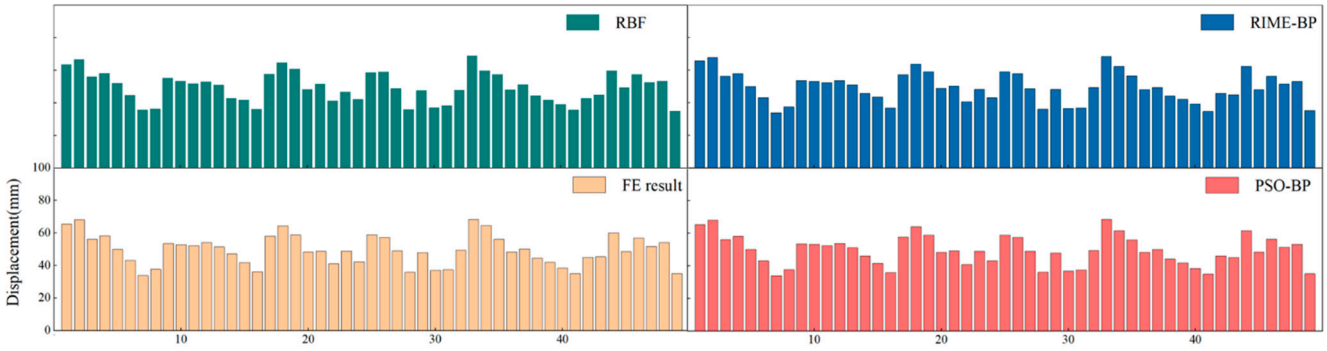


Figure 9. Comparison of Neural Network Predictions and Simulation Results.

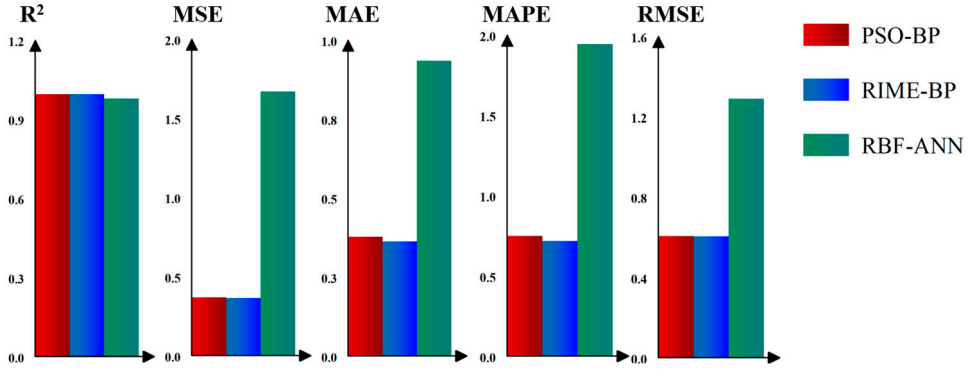


Figure 10. Comparison of different models (within the defined limits).

By comparison, we can see that all the prediction models have relatively high prediction accuracy in the design domain, and the PSO-BP and RIME-BP models excel in all the indicators, with R^2 values over 0.995, smaller MSE and MAE values, and higher

prediction accuracy. In contrast, RBF has lower R^2 values, higher MSE and MAE values, and relatively poorer prediction accuracy. However, it is not enough to just look at these evaluation indexes; we then exclude the previous samples as training samples from the design domain to re-sample 10 groups of random samples. These 10 groups of random samples after the simulation results are shown in Table 8, and then compared with the results obtained by each neural network model prediction results, as shown in Figure 11.

Table 8. Experimental results (within the defined limits).

Run	Velocity (Km/h)	Radius (mm)	Thickness (mm)	Displacement (mm)
#1	20	70	2.6	35.033
#2	24	70	2.4	44.256
#3	24	60	2.2	45.776
#4	32	40	2.2	61.287
...	...	...	...	...
#10	36	80	2.6	58.764

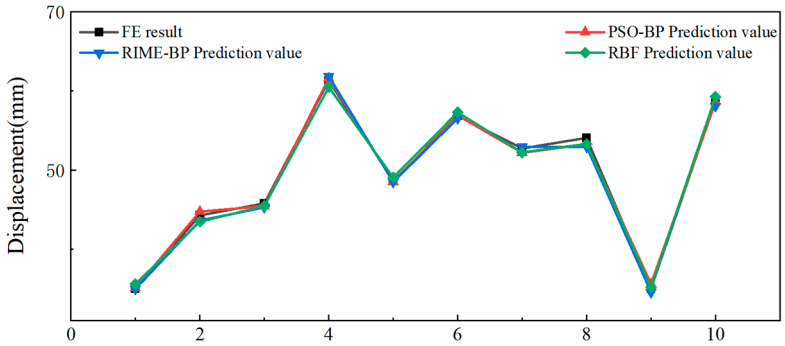


Figure 11. Comparison of prediction results from different models (within the defined limits).

By comparing the prediction results of each model, it can be seen that the prediction accuracy of each model in the design domain is relatively high. Therefore, after analyzing the prediction results within the defined limits, we also need to compare the prediction accuracy beyond the defined limits. A model prediction is considered distorted when the maximum percentage error in the model prediction exceeds 5%.

In order to investigate the accuracy of prediction Beyond the defined limits, we extended the range of three variables. The speed range was extended from 20–36 Km/h to 44 Km/h, the thickness range to 3.6 mm, and the radius range was extended to 100 mm. Then we continued to take 16 sets of samples from the samples after the extension by the orthogonal experimental method for the experiments [41], and the 16 samples obtained by using the orthogonal experimental design are shown in Table 9, and at this time, the prediction accuracy for each model is provided in Table 10 and Figure 12.

The results show that the RIME-BP model has the best performance in all the metrics, with R^2 reaching 0.9340, indicating its high fitting effect. A total of 1.6499 mm^2 for MSE, 0.9715 mm for MAE, and 1.7726% for MAPE show the model's excellent performance in reducing the error and improving the accuracy. A total of 1.2041 mm for RMSE further proves its prediction accuracy. The RMSE was 1.2041 mm, which further proved the accuracy of its prediction. In contrast, the PSO-BP model has an R^2 of 0.9242, which is better, but the MSE (1.9209 mm^2) and RMSE (1.3859 mm) are slightly higher than those of RIME-BP, indicating that the model does not handle large errors as well as RIME-BP. MAE and MAPE are still kept at a low level, which indicates that the model has good stability. R^2 is 0.9231, which is relatively poor, and the MSE (2.2219 mm^2) and RMSE (1.4906 mm) are high, indicating that the prediction error of RBF-ANN is large, and the accuracy is not

as good as PSO-BP and RIME-BP. Overall, the RIME-BP model performs the best in all the error indexes.

Table 9. Orthogonal experimental samples (outside design domain).

Run	Velocity (m/s)	Radius (mm)	Thickness (mm)
#1	38	85	3.0
#2	38	90	3.2
...	...	...	...
#16	44	85	3.6

Table 10. Comparison of different models (outside design domain).

Model	R^2	MSE (mm)	RMSE (mm)	MAE (mm)	MAPE (%)
PSO-BP	0.9242	1.9209	1.3859	1.0867	1.9660
RIME-BP	0.9340	1.6499	1.2041	0.9715	1.7726
RBF	0.9231	2.2219	1.4906	1.0540	2.1063

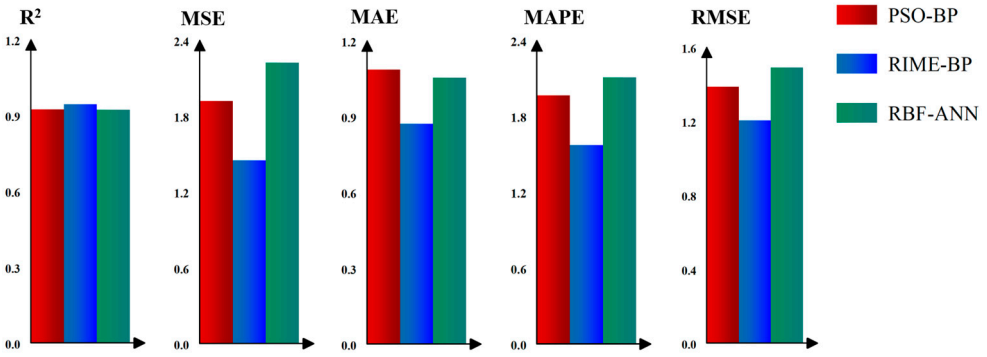


Figure 12. Comparison of different models (outside the defined limits).

5. Conclusions

In this study, three prediction models based on neural network algorithms for the bottom shell of battery pack deformation under frontal collision conditions were developed. And the validity of these models was verified through a series of steps. First, a finite element model of the battery pack system (BPS) is developed. The accuracy of the model was verified through constrained modal analysis tests to ensure the reliability of the model in representing real-world scenarios. Subsequently, a representative sample of experiments was systematically collected to capture a variety of data and simulated using optimal Latin hypercube sampling techniques, thus ensuring efficient and comprehensive sampling of the design space.

Next, various types of neural network models are employed to establish predictive models, each tailored to account for specific factors influencing the deformation of the BPS during collisions. The performance of each model is rigorously assessed by comparing the prediction accuracy using different error functions. The results demonstrate that, even when tested beyond the defined limits, all three models continue to yield highly accurate predictions. Among them, the RIME-BP model consistently outperforms the other models, showcasing its superior predictive capability.

In conclusion, the neural network-based prediction models developed in this study not only serve as valuable tools for forecasting the mechanical safety of the BPS but also provide critical data to support the optimal design and enhancement of battery pack structures. These models have the potential to contribute significantly to the design of safer, more efficient battery packs, particularly in the context of electric vehicle safety.

Author Contributions: Data curation, J.W.; methodology, O.C.; resources, Z.Z. (Zhiwei Zhao) and H.B.; software, J.W.; writing—original draft, J.W.; writing—review and editing, Z.Z. (Zhenfei Zhan). All authors have read and agreed to the published version of the manuscript.

Funding: This paper is supported by the Open Fund of National Key Laboratory of Intelligent Vehicle Safety Technology (IVSTSKL-202305), the Jiangsu Materials Big Data Public Technical Service Platform (BM2021007), the Industrial Application Materials Big Data Platform project, and Chongqing Jiaotong University-Yangtze Delta Advanced Material Research Institute Provincial-level Joint Graduate Student Cultivation Base (JDLHPYJD2021008).

Institutional Review Board Statement: Not applicable.

Informed Consent Statement: Not applicable.

Data Availability Statement: The original contributions presented in the study are included in the article, further inquiries can be directed to the corresponding author.

Conflicts of Interest: Authors Zhiwei Zhao and Huanhuan Bao are employed by the company China Automotive Engineering Research Institute Co., Ltd. The remaining authors declare that the research was conducted in the absence of any commercial or financial relationships that could be construed as a potential conflict of interest.

References

1. Tian, J.; Wang, P.; Zhu, D. Overview of Chinese new energy vehicle industry and policy development. *Green Energy Resour.* **2024**, *2*, 100075. [CrossRef]
2. Wang, S.; Shi, L. EV diffusion promotion analysis under different charging market structure. *Technol. Forecast. Soc. Chang.* **2024**, *208*, 123730. [CrossRef]
3. Zhao, J.; Feng, X.; Pang, Q.; Fowler, M.; Lian, Y.; Ouyang, M.; Burke, A.F. Battery safety: Machine learning-based prognostics. *Prog. Energy Combust. Sci.* **2024**, *102*, 101142. [CrossRef]
4. Wen, J.; Yu, Y.; Chen, C. A review on lithium-ion batteries safety issues: Existing problems and possible solutions. *Mater. Express* **2012**, *2*, 197–205. [CrossRef]
5. Gharehghani, A.; Rabiei, M.; Mehranfar, S.; Saeedipour, S.; Andwari, A.M.; García, A.; Reche, C.M. Progress in battery thermal management systems technologies for electric vehicles. *Renew. Sustain. Energy Rev.* **2024**, *202*, 114654. [CrossRef]
6. Wei, Y.; Li, K.; Liu, Z.; Xie, Y.; Song, Z.; Yue, H. Modeling and control strategy optimization of battery pack thermal management system considering aging and temperature inconsistency for fast charging. *Appl. Therm. Eng.* **2024**, *256*, 124153. [CrossRef]
7. Awasthi, S. A review on the optimization of electrolytes to enhance lithium-ion batteries' safety and performance under abuse conditions. *J. Energy Storage* **2024**, *100*, 113439. [CrossRef]
8. Mo, W.; Lin, Y.; Li, J.; Lian, C.; Liu, H. An optimized hybrid battery pack with high energy density and high safety. *Chem. Eng. Sci.* **2024**, *297*, 120290. [CrossRef]
9. Xing, Y.; Li, Q.M. Evaluation of the mechanical shock testing standards for electric vehicle batteries. *Int. J. Impact Eng.* **2024**, *194*, 105077. [CrossRef]
10. Xia, Y.; Chen, G.; Zhou, Q.; Shi, X.; Shi, F. Failure behaviours of 100% SOC lithium-ion battery modules under different impact loading conditions. *Eng. Fail. Anal.* **2017**, *82*, 149–160. [CrossRef]
11. Zheng, G.; Tan, L.; Tian, G.; Yang, B.; Li, Q.; Sun, G. Dynamic crashing behaviors of prismatic lithium-ion battery cells. *Thin-Walled Struct.* **2023**, *192*, 110902. [CrossRef]
12. Xia, Y.; Wierzbicki, T.; Sahraei, E.; Zhang, X. Damage of cells and battery packs due to ground impact. *J. Power Sources* **2014**, *267*, 78–97. [CrossRef]
13. Li, J.; Chen, Z.; Xie, Y.; Wen, H.; Cai, C.; Wang, H. Lithium Iron Phosphate Battery Failure Under Vibration. *World Electr. Veh. J.* **2024**, *15*, 548. [CrossRef]
14. Zhu, Q.; Liang, K.; Zhou, X. Research on Thermal Runaway Characteristics of High-Capacity Lithium Iron Phosphate Batteries for Electric Vehicles. *World Electr. Veh. J.* **2024**, *15*, 147. [CrossRef]
15. Shi, C.; Zhu, D.; Zhang, L.; Song, S.; Sheldon, B.W. Transfer Learning Prediction on Lithium-Ion Battery Heat Release Under Thermal Runaway Condition. *Nano Res. Energy* **2024**, *3*, e9120147. [CrossRef]
16. Wang, W.; Dai, S.; Zhao, W.; Wang, C.; Ma, T. Design optimization of a novel negative Poisson's ratio non-module battery pack system considering crashworthiness and heat dissipation. *Compos. Struct.* **2021**, *275*, 114458. [CrossRef]
17. Kisters, T.; Keshavarzi, M.; Kuder, J.; Sahraei, E. Effects of electrolyte, thickness, and casing stiffness on the dynamic response of lithium-ion battery cells. *Energy Rep.* **2021**, *7*, 6451–6461. [CrossRef]

18. Zhang, Q.; Han, S.; Abed, A.M.; Basem, A.; El-Sharkawy, M.R.; Salah, B.; Mahariq, I. Enhancing battery pack safety against cone impact using machine learning techniques and Gaussian noise. *Process Saf. Environ. Prot.* **2024**, *191*, 448–465. [CrossRef]
19. Chen, X.; Yuan, Q.; Wang, T.; Ji, H.; Ji, Y.; Li, L.; Liu, Y. Experimental study on the dynamic behavior of prismatic lithium-ion battery upon repeated impact. *Eng. Fail. Anal.* **2020**, *115*, 104667. [CrossRef]
20. Chen, P.; Xia, Y.; Zhou, Q.; Liu, S. Staggered layout of battery cells for mitigating damage in side pole collisions of electric vehicles. *eTransportation* **2023**, *16*, 100238. [CrossRef]
21. Wang, W.; Zhang, T.; He, Y.; Zhang, W.; Xu, X.; Ju, F. Uncertainty bottom impact optimization of power battery pack with 3D star-shaped auxetic structure. *Appl. Soft Comput.* **2024**, *161*, 111742. [CrossRef]
22. Xu, D.; Pan, Y.; Zhang, X.; Dai, W.; Liu, B.; Shuai, Q. Data-Driven Modelling and Evaluation of a Battery-Pack System's Mechanical Safety Against Bottom Cone Impact. *Energy* **2024**, *290*, 130145. [CrossRef]
23. Li, R.; Pan, Y.; Zhang, X.; Dai, W.; Liu, B.; Li, J. Mechanical safety prediction of a battery-pack system under low-speed frontal impact via machine learning. *Eng. Anal. Bound. Elem.* **2024**, *160*, 65–75. [CrossRef]
24. Bin Liu, R.; Villavicencio, P.T.; Pedersen, C.G. Soares. Analysis of structural crashworthiness of double-hull ships in collision and grounding. *Mar. Struct.* **2021**, *76*, 102898. [CrossRef]
25. Körmöczi, D.; Kiss, P. Comparison of selected tire-terrain interaction models from the aspect of accuracy and computational intensity. *J. Terramechanics* **2025**, *117*, 101030. [CrossRef]
26. Shen, Z.; Chouvion, B.; Thouverez, F.; Beley, A. Enhanced 3D solid finite element formulation for rotor dynamics simulation. *Finite Elem. Anal. Des.* **2021**, *195*, 103584. [CrossRef]
27. Li, R.; Zhao, Z.; Bao, H.; Pan, Y.; Wang, G.; Liu, B.; Liao, T.; Li, J. Bio-inspired honeycomb structures to improve the crashworthiness of a battery-pack system. *Eng. Fail. Anal.* **2024**, *158*, 108041. [CrossRef]
28. Xiong, Y.; Pan, Y.; Wu, L.; Liu, B. Effective weight-reduction and crashworthiness analysis of a vehicle's battery-pack system via orthogonal experimental design and response surface methodology. *Eng. Fail. Anal.* **2021**, *128*, 105635. [CrossRef]
29. Miao, F.; Jin, Y. Crashworthiness analysis and structural optimization of thin-walled circular tubes with porous arrays. *Structures* **2024**, *70*, 107811. [CrossRef]
30. Kwag, S.; Eem, S.; Kwak, J.; Lee, H.; Oh, J.; Koo, G.-H. Improvement on optimal design of dynamic absorber for enhancing seismic performance of nuclear piping using adaptive Kriging method. *Nucl. Eng. Technol.* **2022**, *54*, 1712–1725. [CrossRef]
31. Bayar, G.; Hambarci, G. Improving measurement accuracy of indoor positioning system of a Mecanum wheeled mobile robot using Monte Carlo-Latin hypercube sampling-based machine learning algorithm. *J. Frankl. Inst.* **2023**, *360*, 13994–14021. [CrossRef]
32. Masoomzadeh, M.; Basim, M.C.; Chenaghlou, M.R.; Khajehsaeid, H. Probabilistic performance assessment of eccentric braced frames using artificial neural networks combined with correlation Latin hypercube sampling. *Structures* **2023**, *48*, 226–240. [CrossRef]
33. Wu, X.; Yang, Y.; Li, K.; Xu, Y.; Peng, J.; Chi, B.; Wang, Z.; Li, X. Performance prediction of gasification-integrated solid oxide fuel cell and gas turbine hybrid systems using PSO-BP neural network. *Renew. Energy* **2024**, *237*, 121711. [CrossRef]
34. Zhang, M. Classification Prediction of Rockburst in Railway Tunnel Based on Mixed PSO-BP Model. *Geofluids* **2022**, *2022*, 4538927. [CrossRef]
35. Shi, J.; Zhang, Y.; Sun, Y.; Cao, W.; Zhou, L. Tool Life Prediction of Dicing Saw Based on PSO-BP Neural Network. *Int. J. Adv. Manuf. Technol.* **2022**, *123*, 4399–4412. [CrossRef]
36. Qu, Z.; Mao, W.; Zhang, K.; Zhang, W.; Li, Z. Multi-Step Wind Speed Forecasting Based on Hybrid Decomposition and Improved BP Neural Network. *Renew. Energy* **2019**, *133*, 919–929. [CrossRef]
37. Su, H.; Zhao, D.; Heidari, A.A.; Liu, L.; Zhang, X.; Mafarja, M.; Chen, H. RIME: A physics-based optimization. *Neurocomputing* **2023**, *532*, 183–214. [CrossRef]
38. Li, J.; Wang, Q.; Zhang, H. An efficient multilayer RBF neural network and its application. *J. Neural Comput. Appl.* **2022**, *34*, 4133–4150. [CrossRef]
39. Erzin, S. Using radial basis artificial neural networks to predict radiation hazard indices in geological materials. *Environ. Monit. Assess.* **2024**, *196*, 315. [CrossRef] [PubMed]
40. Zhang, L.; Chen, J.; Zhao, S.; Chen, Y.; Song, H.; Liu, J. Research of cooling tower filler based on radial basis function artificial neural network (RBF ANN). *Energy Sci. Eng.* **2023**, *11*, 2885–2898. [CrossRef]
41. Yin, J.; Lei, Q.; Li, X.; Zhang, X.; Meng, X.; Jiang, Y.; Tian, L.; Zhou, S.; Li, Z. A novel neural network-based alloy design strategy: Gated recurrent unit machine learning modeling integrated with orthogonal experiment design and data augmentation. *Acta Mater.* **2023**, *243*, 118420. [CrossRef]

Disclaimer/Publisher's Note: The statements, opinions and data contained in all publications are solely those of the individual author(s) and contributor(s) and not of MDPI and/or the editor(s). MDPI and/or the editor(s) disclaim responsibility for any injury to people or property resulting from any ideas, methods, instructions or products referred to in the content.